RESEARCH ARTICLE

Ligand Electronics Dictate Geometry, Stability, and Cancer Cell Toxicity in Carbon-Stabilized Gold(III) Macrocycles

Justin C. Holmes[1] | Arinzechukwu Egwu[1] | Sean Parkin[1] | Sanjay Dutta[1] | Sashen Ruhunage[1,2] | Chad Risko[1,2] | Samuel G. Awuah[1,3,4]

[1]Department of Chemistry, University of Kentucky, Lexington, Kentucky, USA | [2]Center for Applied Energy Research, University of Kentucky, Lexington, Kentucky, USA | [3]Department of Pharmaceutical Sciences, College of Pharmacy, University of Kentucky, Lexington, Kentucky, USA | [4]Markey Cancer Center, University of Kentucky, Lexington, Kentucky, USA

Correspondence: Samuel G. Awuah (awuah@uky.edu)

Received: 17 December 2025 | **Revised:** 1 March 2026 | **Accepted:** 2 March 2026

Keywords: anticancer | electronics | gold macrocycles | gold(III) complexes | macrocycles

ABSTRACT

Strategies for rationally designing gold-based chemotherapeutics remain limited by an incomplete understanding of how ligand electronics shape structure and biological function. Here, we establish a direct link between σ-donor strength, geometric distortion, and anticancer activity across a series of carbon-stabilized Au(III) bisphosphine macrocycles derived from *N*,*N*′-(1,2-phenylene)bis(2-(diphenylphosphino)benzamide) ($dppbH_2$) and electronically tuned cyclometalated [C^N] templates. Systematic installation of substituents that modulate σ-donation to Au(III) produces predictable shifts in Au—C and Au—P bond lengths, *trans* bite angles, and square planar deformation. σ-donor character of complexes influences geometric distortion, aqueous stability, and up to an order-of-magnitude higher cytotoxicity in triple-negative breast cancer and estrogen receptor–positive models compared to cisplatin. Mechanism of action studies supports acute mitochondrial uncoupling and mtROS production, leading to cell death by this class of compounds. This electronic–structural–biological correlation provides a rare, experimentally validated design principle for Au(III) scaffolds and positions electronically tuned macrocycles as a chemically tractable platform for targeting intracellular pathways.

1 | Introduction

Macrocyclization is a well-established strategy in medicinal chemistry for improving the stability, selectivity, and cellular permeability of bioactive molecules [1–4]. Although biology routinely employs metal-containing macrocycles such as heme and cobalamins, the intentional use of metal-based macrocycles in therapeutic or probe development remains comparatively underexplored. Organometallic macrocycles, particularly those containing direct metal–carbon bonds, offer the ability to tune redox properties, geometry, and physicochemical behavior in ways that are inaccessible to purely organic scaffolds. Expanding such architectures is an attractive route toward designing metallodrugs with controllable reactivity and target selectivity.

Gold(III) complexes have gained increasing attention as potential anticancer agents due to their high reduction potential, relativistic stabilization, and square planar d^8 configuration, which is isoelectronic with the Pt(II) center of cisplatin [5–10]. However, despite their promise, most Au(III) complexes do not progress beyond preclinical evaluation, largely because of insufficient stability under biological conditions or an incomplete understanding of their mechanisms of action [7, 11]. Incorporation of bisphosphine ligands provides an effective strategy to address these challenges, as strong σ-donating phosphines enhance Au–P covalency, reinforce square planar geometry, and increase resistance to reduction and ligand exchange under physiological conditions. Moreover, bidentate phosphines introduce defined bite angles [12] and electronic tunability, allowing systematic modulation of the metal center while maintaining structural rigidity [13]. We recently reported a family of carbon-stabilized gold(III) bisphosphine macrocycles that exhibit robust activity in breast cancer cell models and engage defined intracellular targets [14], motivating the need for a rational

design framework linking structure, electronic properties, and biological function.

In this work, we establish such a structure–activity relationship by systematically modifying the aryl ligand embedded within the macrocyclic scaffold. Substituent-based tuning of σ-donor strength provides a direct means to influence metal–ligand bond metrics, *trans* bite angle, and square planar distortion, which is an effect rooted in the well-described *trans* influence of d^8 metal complexes [15–20]. However, in Au(III) macrocycles, this phenomenon is amplified by the strongly σ-donating carbon anchor of the (C^N) unit, which raises the energy of the $5d^{x2-y2}$ orbital and increases the susceptibility of the metal center to additional donor perturbation [21, 22]. As a result, electronic effects extend beyond a single metal–ligand axis, altering covalency, macrocyclic rigidity, and ultimately redox stability and biological activity. Both strong σ-donor ligands and macrocyclic constraint have independently been shown to stabilize the Au(III) oxidation state [23–25], suggesting a synergistic design space not yet fully explored.

Here, we show that electronically diverse substituents on the arylligand enable predictive control over geometry, solution stability, and cytotoxic potency in triple-negative and estrogen receptor–positive breast cancer cell lines. This study establishes an electronic–structural–biological correlation for organogold(III) macrocycles and highlights σ-donor modulation as a generalizable strategy for advancing nonplatinum metallotherapeutics.

2 | Results and Discussion

2.1 | Rationale, Synthesis, and Characterization of Gold(III) Macrocycles

To investigate how ligand σ-donor strength governs the structural and biological properties of carbon-stabilized Au(III) macrocycles, we designed a modular synthetic route that enables systematic variation of the cyclometalated (C^N) fragment while maintaining a constant bisphosphine macrocyclic framework. Utilization of the bisphosphine ligand—$dppbH_2$ was inspired by groups who have used the ligand to form macrocyclic complexes with other transition metals such as Pd(II) [26], Pt(II) [26], Ru(II) [27], Ni(II) [28], and Rh(I) [29]. The $dppbH_2$ was prepared through an amide coupling reaction between *o*-phenylenediamine and 2-diphenylphosphinobenzoic acid (DPPBA). Use of HOBt as an activating additive minimized competitive *O*-acylation and afforded the desired diamide. The corresponding cyclometalated Au(III) precursors were synthesized by direct C–H activation of substituted phenylpyridine scaffolds with $HAuCl_4{\cdot}3H_2O$ in water under in a pressure tube at 120°C–130°C. Notably, the reaction rate of the cyclometalation correlated with the bridging heteroatom (X = NH, O, CH_2, None) within the arylpyridine framework shown in Scheme 1. Specifically, the formation [C^N] Au(III)Cl_2 was influenced by the donor character of the bridging atom(s). The reaction for the formation of NH-derived [C^N] Au(III)Cl_2 was 1 h, whereas the O-bridging required 4–5 h and the methylene- and no-bridge cyclometalated complexes required 24 h. This trend correlates with the increasing σ-donor ability of the bridge atom (NH > O > CH_2 ≥ None), which facilitates metalation by enhancing electron density at the cyclometalating carbon and lowering the activation barrier for Au–C bond formation. These data reinforce the notion that donor-modulated C^N cyclometalation is kinetically, not just thermodynamically, controlled which is an effect consistent with the increased *trans* influence exerted by stronger σ-donors in d^8 Au(III) systems.

Further, we pursued reactions of the [C^N] Au(III)Cl_2 with the phenylene-supported bisphosphine ligand with a wide bite angle to generate organogold(III) macrocycles with *trans* phosphine ligation (Scheme 1). Purification was by silica gel flash column chromatography and compounds were fully characterized by spectroscopy and structural elucidation by X-ray. Full spectroscopic (^1H, ^{31}P NMR), HRMS, and single-crystal X-ray analysis confirmed macrocyclization and the expected square planar Au(III) coordination geometry. Comparative structural metrics are discussed in the following section.

2.2 | Structural Analysis

Detailed structural and geometric analysis of Au(III) macrocycles remain heavily underexplored. Here, we employed X-ray crystallography and density functional theory (DFT) calculations to elucidate information pertaining to macrocyclic bonding, structure, and geometry. First, single crystals suitable for X-ray diffraction were grown by slow diffusion of diethyl ether into saturated solutions of 1:1 (v/v) $CHCl_3$/MeOH (Figure 1).

Structural analysis of the macrocycles (Table 1) revealed clear electronic trends in metal–ligand bonding as a function of

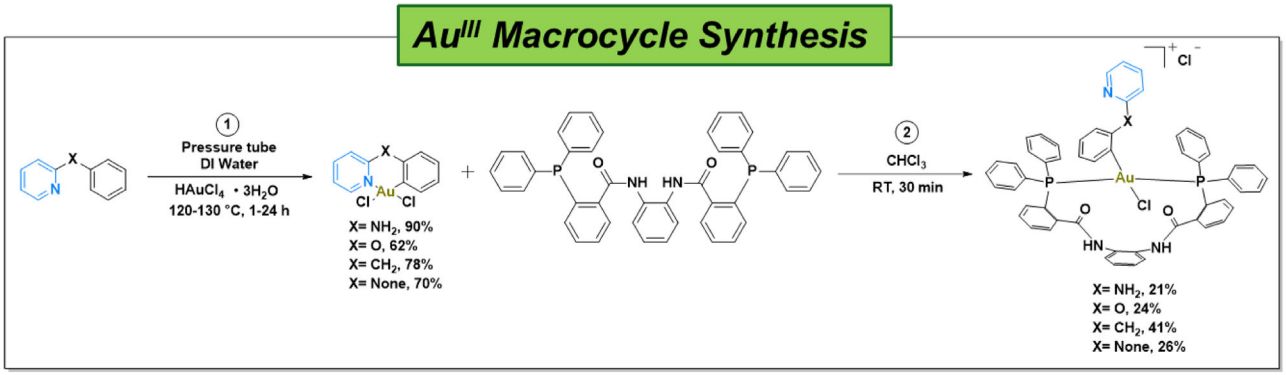

SCHEME 1 | Synthetic scheme for the synthesis of benzene-supported bisphosphine gold(III) macrocycles. 1. Synthesis of Au(III) cyclometalated complexes. 2. Synthesis of benzene-supported bisphosphine gold(III) macrocycles (**AuBz1–AuBz4**).

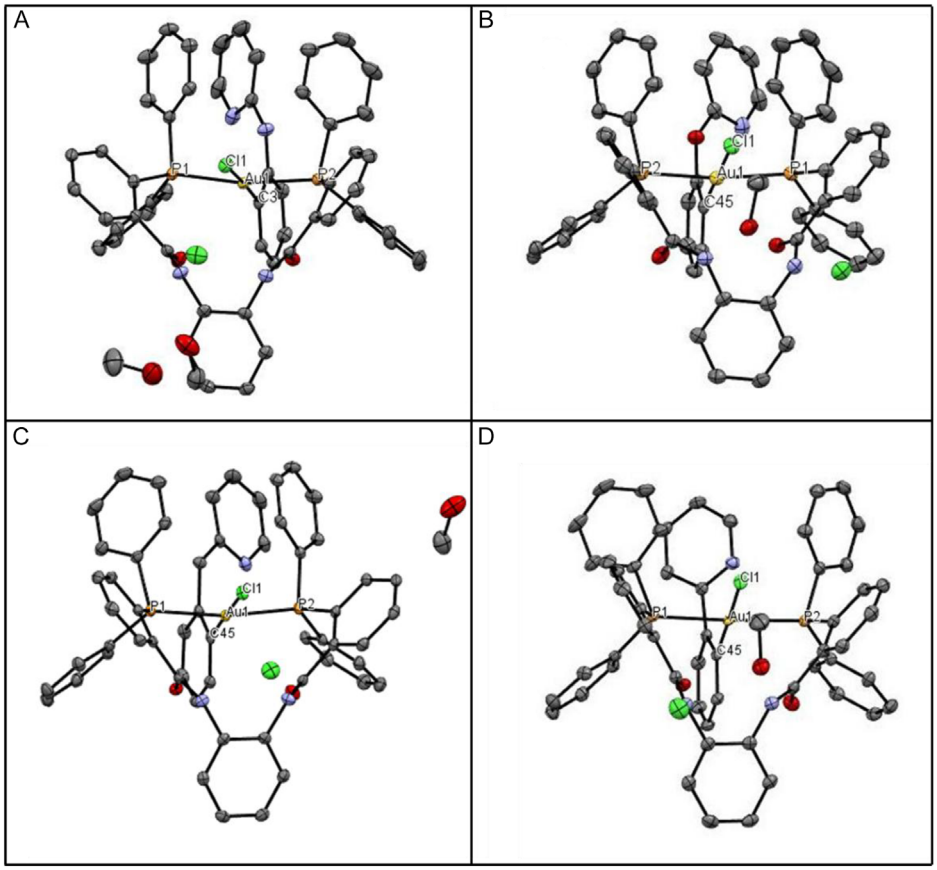

FIGURE 1 | X-ray single crystals of the gold(III) bisphosphine macrocycles. (A) **AuBz1**; (B) **AuBz2**, (C) **AuBz3**, and (D) **AuBz4**. Thermal ellipsoids are shown at the 50% probability level. Hydrogen molecules are omitted for clarity. Only one representative molecule from the asymmetric unit is shown.

TABLE 1 | Macrocycle bond lengths (Å) of Au–C, Au–Cl, Au–P, and average Au–P as derived from X-ray crystallography and DFT calculations (in parenthesis).

	Bond length (Å)			
Bond	**AuBz1**	**AuBz2**	**AuBz3**	**AuBz4**
Au1—C45	2.0344 ± 0.0017 (2.043)	2.037 ± 0.002 (2.036)	2.0432 ± 0.0017 (2.051)	2.0382 ± 0.0019 (2.054)
Au1—Cl1	2.3706 ± 0.0004 (2.503)	2.3667 ± 0.0006 (2.500)	2.3753 ± 0.0004 (2.511)	2.3727 ± 0.0005 (2.515)
Au1—P1	2.3740 ± 0.0004 (2.460)	2.3772 ± 0.0006 (2.472)	2.3976 ± 0.0004 (2.473)	2.3870 ±0.0005 (2.467)
Au1—P2	2.3927 ± 0.0004 (2.470)	2.3711 ± 0.0006 (2.460)	2.3744 ± 0.0004 (2.462)	2.3922 ± 0.0005 (2.462)
Avg. P—Au	2.3833 (2.465)	2.3741 (2.466)	2.3860 (2.467)	2.3896 (2.464)

arylligand donor strength. Experimentally, the Au—C bond length decreases in the order AuBz3 > AuBz4 > AuBz2 > AuBz1, showing that more electron-donating bridge atoms (NH—AuBz1 and O—AuBz2) strengthen and contract the aryl C–Au linkage. This is consistent with increased electron donation into the aryl ring, which enhances covalency at the metal–carbon bond. Although these measurements derive from solid-state structures, it is important to note that metal–ligand distances in solution may be modulated by additional factors including solvent coordination, hydrogen bonding, conformational dynamics, and ion pairing, which collectively tune the effective electronic environment of Au(III) complexes. Interestingly, despite classical expectations that stronger σ-donors exert a larger *trans* influence and lengthen the *trans* Au—Cl bond, we observed the opposite behavior. AuBz1 and AuBz2 exhibit shorter Au–Cl distances relative to AuBz3 and AuBz4. A similar contraction is seen for the average Au—P bond lengths, which are shortest for the most electron-rich complexes.

Second, DFT calculations performed at the ωB97XD/LANL2DZ (CPCM ε = water) level of theory generally reproduce the experimentally observed trend toward shorter Au—ligand bond lengths with increasing donor strength. However, while the calculations capture the overall magnitude and directionality of bond contraction, discrepancies arise in the relative ordering of bond lengths across the series, particularly for the Au–C and averaged Au–P distances. These deviations indicate that subtle intercomplex structural trends are sensitive to solid-state and

environmental effects not fully accounted for in the computational model.

To gain further insight into the origins of the Au—L bonding trends, frontier molecular orbital (FMO) analyses were carried out on the DFT-optimized structures (Table 2). FMO analyses show that the highest occupied molecular orbitals (HOMOs) of AuBz1 (−7.74 eV) and AuBz2 (−8.63 eV) are distributed across the π orbitals of both aryl rings of the cycometalated ligand (Figure 2). A different picture emerges, however, for AuBz3 (−8.66 eV) and AuBz4 (−8.63 eV), as both systems present the HOMO spread across the π system of the arylligand and the phosphine ligands; notably, the portion of the HOMO on aryl ligand of AuBz4 is delocalized across the π system while that on the aryl ligand of AuBz3 is localized on the phenyl ring, enabling electron density to be directly pulled to the Au(III) via the C—Au σ-bond and preventing any redistribution to the pyridine ring. This is consistent with calculated Mulliken charges on the Au(III), where Au of AuBz4 has the least electron density of the series, whereas for AuBz3 it has the most (Table S5). The macrocyle LUMOs, on the other hand, exhibit similar behavior across all four systems, with minor variation in the LUMO energies. Taken together, these data indicate that increasing electron donor strength of the aryl ligand induces a global contraction of all four Au—L bonds in these macrocycles. This behavior is distinct from traditional *trans* influence patterns suggesting a cooperative electronic effect unique to this bisphosphine macrocyclic framework, where enhanced ligand donation stabilizes the d^8 Au(III) center through increased covalency rather than bond liability.

To quantify the extent of deviation from an ideal square planar geometry, the two *trans* angles (C45–Au–Cl and P1–Au–P2) and the distribution of *cis* angles were examined for each macrocycle, and the square planarity index was calculated (Table 3, Equation (1)). Experimentally, the average deviation of the *trans* angles from 180°, as well as the square planarity index (T_4 closer to 0 = more square planar), follows a similar trend: AuBz4 < AuBz2 < AuBz3 < AuBz1. The DFT-derived geometries reflect the same correlation between *trans* angle deviation and square planarity, but with a slight alteration in ordering: AuBz4 < AuBz3 < AuBz1 < AuBz2. In each case, AuBz4 is the most square planar and the complexes with the most electron-donating cyclometated ligands (experimental—AuBz1 and DFT—AuBz2) are the least square planar. This indicates that both electronic donation and geometric strain govern the final coordination geometry. Consistent with this, the *cis* angle range decreases as the P–Au–P *trans* angle becomes more distorted, suggesting that as the *trans* angle is forced away from 180°, the *cis* angles may compensate by collapsing toward a uniform, constrained bite.

TABLE 2 | DFT-derived HOMO and LUMO energies (eV) and HOMO–LUMO energy gaps (eV) of the four macrocyclic complexes.

Compound	HOMO energy, eV	LUMO energy, eV	HOMO-LUMO Energy gap, eV
AuBz1	−7.74	−1.60	6.13
AuBz2	−8.63	−1.62	7.01
AuBz3	−8.66	−1.56	7.10
AuBz4	−8.63	−1.53	7.10

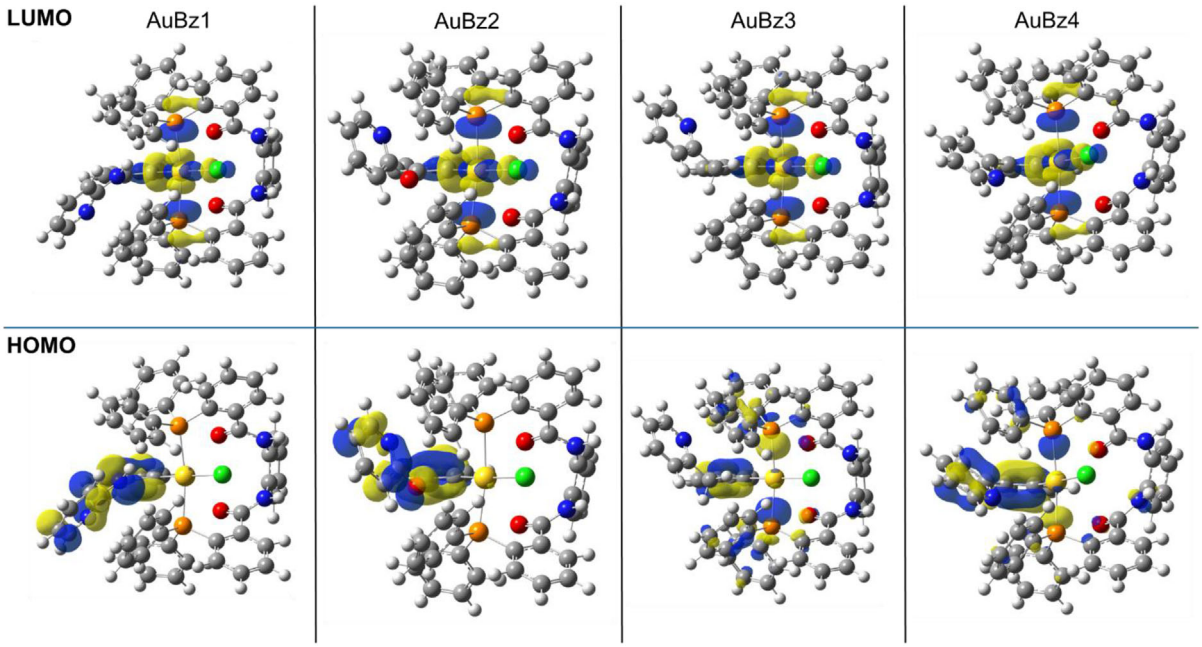

FIGURE 2 | Pictorial representations of the respective HOMO and LUMO of the macrocyclic complexes as determined at the ωB97X-D/LANL2DZ (CPCM water) level of theory (isovalue = 0.04).

TABLE 3 | Select geometric parameters, correlated to macrocycle stability, as derived from X-ray crystallography and DFT calculations (in parentheses).

Compound	Avg. *Trans* angle deviation, °	*Cis* angle range, °	*Cis* angle range Δ	T_4
AuBz1	7.13 (5.52)	89.04 - 91.50 (88.42–91.46)	2.46 (3.04)	0.101 (0.078)
AuBz2	4.31 (7.49)	88.68 - 91.20 (88.36–91.41)	2.52 (3.05)	0.061 (0.106)
AuBz3	5.86 (5.24)	89.51 - 91.04 (88.35–92.72)	1.53 (4.37)	0.083 (0.074)
AuBz4	2.34 (4.98)	88.83 - 92.76 (87.93–92.72)	3.93 (4.79)	0.033 (0.071)

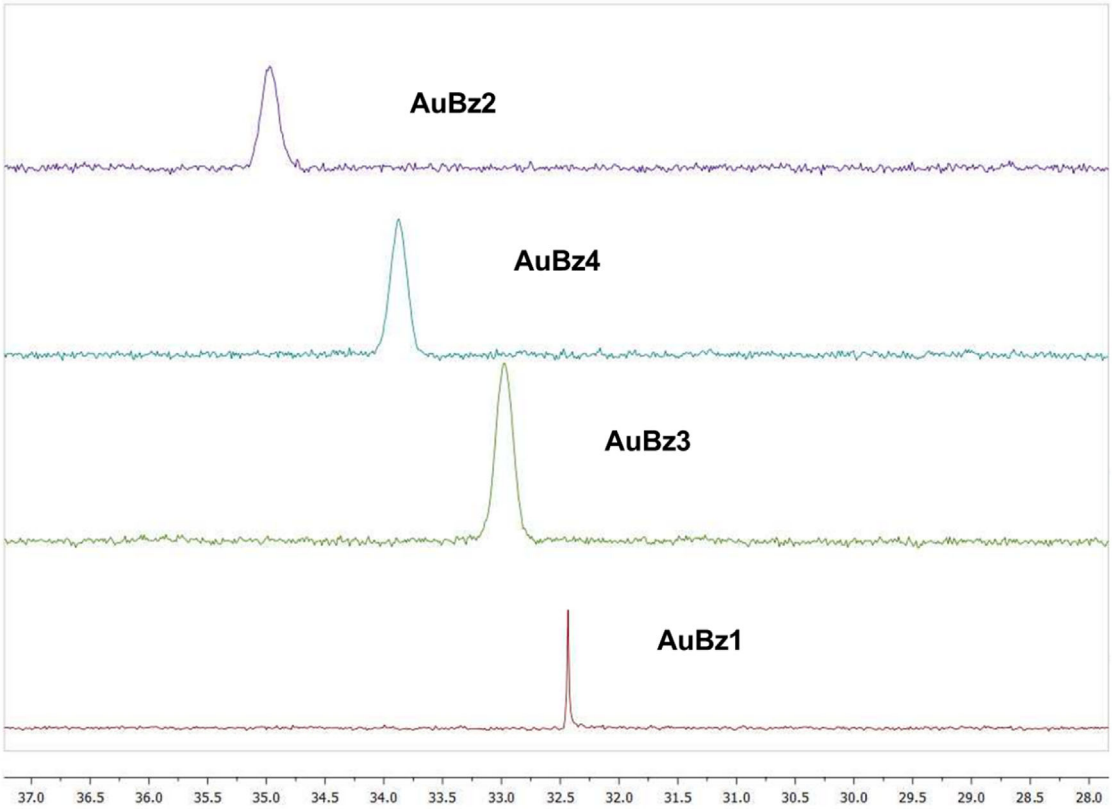

FIGURE 3 | A-^{31}P NMR shifts of AuBz2, AuBz4, AuBz3, and AuBz1 in $CDCl_3$.

Although it appears that an excess of electron donation to the Au(III) center leads to distortion and overall, less square planarity, sufficient electron density must be delivered to the metal to strengthen the Au—C bond and stabilize the complex. Further supporting this, AuBz2 has a short Au—C bond (Table 1), the second lowest *trans* angle deviation, and second-most square planarity (for the experimental structure). Thus, there is a fine balance between enough electron donation to strengthen the Au—C bond, and an excess which distorts the complexes square planar geometry, both of which have implications in complex stability. (Table 3)

$$\tau_4 = \frac{360° - (\alpha + \beta)}{141°} \quad (1)$$

Geometry index equation used to calculate the degree of square planarity. Adopted from Yang et al., 2007 [30].

To further characterize electronic effects of the novel complexes, we examined the chemical shifts of the $\delta(^{31}P)$ NMR. All complexes were prepared in $CDCl_3$ and run at 64 scans on a Bruker NEO Advance 400 MHz spectrometer. Downfield shifts are observed in the ^{31}P NMR spectra in the following order: AuBz2 > AuBz4 > AuBz3 > AuBz1 (Figure 3). The trend suggests chemical shifts increase (deshielding) as gold becomes less able to back-donate electron density to the phosphines. AuBz2 and AuBz4 have Au centers with the least electron density, leading to the least shielding (highest ppm). In support of this claim, we determined the Mulliken charges of crucial atoms within individual complexes (Table S5). Specifically, AuBz2 has the least electron-rich Au (charge ≈0). This implies the weakest Au → P π-back-donation suggestive of weaker back-donation, leading to a smaller excitation energy (ΔE) for P-centered orbital excitations. A smaller ΔE dramatically increases the deshielding paramagnetic term (σ_p), resulting in the highest observed chemical shift (34.97 ppm). AuBz1 and AuBz3 have more negative Au, indicating stronger back-donation, a larger ΔE, more shielding, and thus lower chemical shifts (≈32.7 ppm). Furthermore, there is a significant line narrowing of AuBz1 which may be a result of

a solution state intra/intermolecular H-bonding interactions and could potentially be related to the compounds distinct properties such as instability. AuBz4 sits in the middle, consistent with its slightly positive Au charge but other structural factors modulating the effect. Overall, we demonstrate using X-ray crystallography, DFT, and NMR spectroscopy the electronic impact of aryl donor ligands on structure, geometry, and bonding in tuning organogold(III) macrocycles.

2.3 | Stability and Solution Chemistry

Utilizing high-performance liquid chromatography coupled with mass spectrometry (LC/MS) the stability of the macrocycles was assessed. The HPLC method remained similar for all complexes with a mobile phase of 0–1 min. 100% $H_2O + 0.1\%$ TFA, 1–15 min. 100% ACN + 0.1 FA, and 15–25 min. 100% $H_2O + 0.1\%$ TFA, and the flow rate set to 1 mL/min. The mass spectrometer was operated in positive ESI mode under low-temperature, low-fragmentation conditions. AuBz1 appears to degrade under LC/MS conditions (Figure S21), whereas the others remain intact (Figure S22–S24). A stability study of AuBz2 and AuBz3 was then performed in DMEM, which contains several biologically relevant nucleophiles and reducing agents (e.g., amino acids). The ^{31}P NMR shift trend correlates well with compound stability, where the AuBz2 starts to degrade at around 2–3 hr with a single degradation peak corresponding to one of the P—Au bonds breaking observed on the LC/MS (Figures 4A and S38–S39). However, AuBz3 starts to degrade immediately upon mixing with DMEM, forming two degradation peaks corresponding to both a single P—Au bond breaking, as well as both P—Au bonds breaking (Figures 4B and S29). In the mobile phase comprised of $H_2O + 0.1\%$ TFA and ACN + 0.1 FA, AuBz1, AuBz3, and AuBz4 ionize on the LC/MS to form the $[M]^+$, $[M]^+/2$, [M-Cl]/2, and $[M\text{-}Cl+TFA]^+$ species (Figure S26, S29, and S30), whereas for AuBz2, only the $[M]^+$ species is observed (Figure S27). Furthermore, the most stable compound, AuBz2, demonstrated optimal stability in aqueous solution (Figure S40) and in the presence of L-GSH (5 equiv.) (Figure S41). The other macrocycles were not subjected to these stability conditions. These data further support the notion that electron-donating character of the bridge atom is essential for compound stability, but an excess leads to distortion and instability.

We evaluated the photophysical properties of the four macrocycles by assessing their absorption profile via UV–Vis spectroscopy in DMSO (Figure 5). A stock solution of each complex was prepared and diluted to a final concentration of 25 μM. The samples were then scanned from 600 to 190 nm. The absorbance profile for all complexes remained similar, with low energy transitions at 320–325 nm and higher energy transitions at 260–265 nm. The higher energy absorbances correspond to intraligand transitions of the aryl–Au(III) complexes, and the lower energy absorbances likely correspond to metal-to-ligand or ligand-to-metal transitions [21]. The low energy transitions present a subtle but notable difference in wavelength absorbance maxima, with the more electron rich aryl ligands shifted to longer wavelengths (AuBz1 = 322 nm and AuBz2 = 325 nm) compared to the less electron rich ligands (AuBz3 = 320 nm, AuBz4 = 321.5 nm). This redshifted absorbance is expected, as substituents with a greater +M mesomeric effect shift compound absorbance to longer wavelengths [31]. The intensity of transitions is also dependent on the electron-donating capability of the bridge atom with the AuBz1 being the most intense, followed by the AuBz2, AuBz3, and AuBz4, respectively. However, the relationship between absorbance maxima and electronics should be interpreted with caution, as the difference in absorbance is too little to confidently establish a direct correlation.

2.4 | MTT Cell Viability Assay

The cytotoxicity of the macrocycles was assessed via the MTT cell viability assay across three triple-negative breast cancer cell

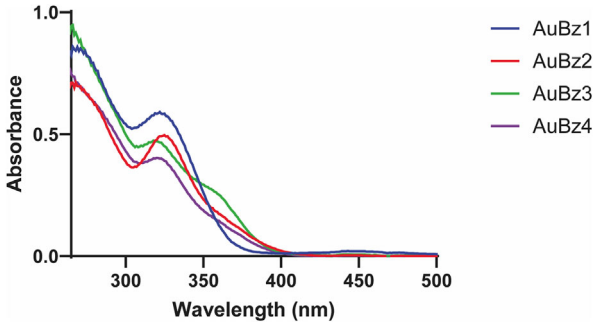

FIGURE 5 | UV–Vis spectra of the four macrocyclic complexes at a concentration of 25 μM in DMSO.

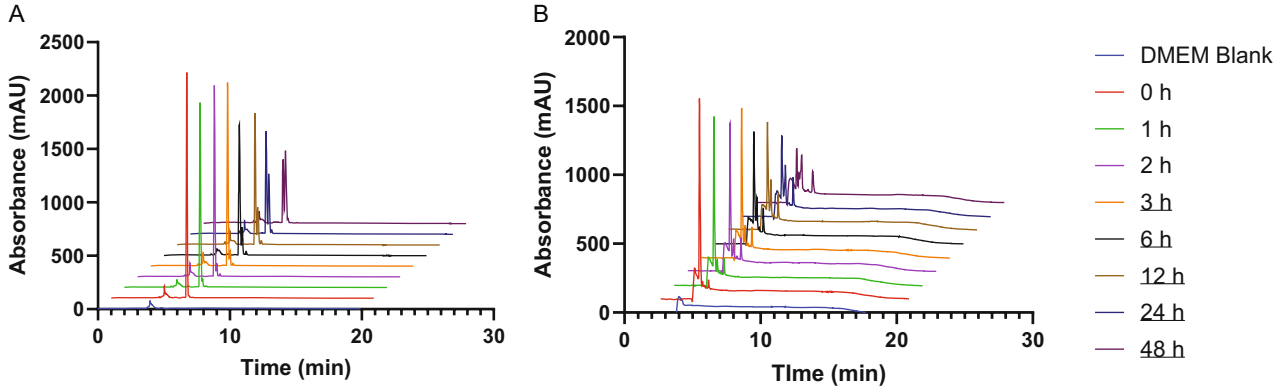

FIGURE 4 | Solution stability of (A) - AuBz2 and (B) – AuBz3 in DMEM for 48 h. Absorbance: λ = 260 nm.

TABLE 4 | IC_{50} values of macrocycles and cisplatin in breast cancer cell lines.

	IC_{50} ± Std Dev., μM			
Compound	**SUM 159**	**MDA-MB 231**	**MDA-MB 468**	**MCF7**
AuBz1	2.05 ± 0.10	3.23 ± 0.04	3.95 ± 0.14	2.56 ± 0.02
AuBz2	1.23 ± 0.07	1.85± 0.05	1.64 ± 0.04	1.11 ± 0.08
AuBz3	1.29 ± 0.07	2.58 ± 0.04	3.12 ± 0.05	1.43 ± 0.05
AuBz4	2.63 ± 0.03	3.89 ± 0.02	3.15 ± 0.05	2.10 ± 0.02
Cisplatin	6.24 ± 0.22	32.98 ± 0.02	6.62 ± 0.06	N/A[a]
dppbH$_2$	N/A[a]	N/A[a]	>100	N/A[a]

[a]N/A: Data not available.

lines SUM159 (RRID:CVCL_5423), MDA-MB-231 (RRID: CVCL_0062), and MDA-MB-468 (RRID:CVCL_0419) as well as MCF-7 (RRID:CVCL_B5 PF), an estrogen receptor–positive breast cancer line. The cells were treated for 72 h, at which point IC_{50} (half-maximal inhibitory concentration) values were determined (Table 4). The data demonstrate a clear correlation between the degree of square planarity, stability, and potency for the macrocycles. Among the series, the AuBz2 macrocycle showed the most favorable balance of geometry, stability, and solubility, and was therefore the most potent compound across all four cell lines. The AuBz3 displayed intermediate activity, reflecting its moderate planarity and stability, whereas both the AuBz1 and AuBz4 analogs were markedly less potent. The reduced activity of the AuBz1 aligns with its substantial geometric distortion and lower solution stability, likely a result of excess electron donation from nitrogen. However, the diminished activity of the AuBz4 complex is consistent with its comparatively poor solubility and reduced electronic reinforcement at the Au(III) center. To ensure cytotoxicity is not coming from the dppbH$_2$ ligand, the IC_{50} of the ligand was determined in MDA-MB 468, where it displayed very minimal activity (Table 4).

All four macrocycles demonstrated greater potency than cisplatin under identical conditions, strongly suggesting that their biological activity may be differentiated from cisplatin. Published work on the few gold(III) macrocyclic compounds developed as anticancer agents display different mechanisms of action such as perturbing redox homeostasis [32], initiating apoptosis [33, 34], or other cytotoxic mechanisms [35], highlighting the therapeutic potential of this class of compounds.

2.5 | AuBz2 Induces Mammosphere Inhibition and Mitochondrial Dysfunction in Cancer Cells

Given the macrocycles have demonstrated cytotoxicity in relevant breast cancer cell lines in a monolayer cell viability assay, we further tested the cytotoxicity of the lead compound—AuBz4 in a mammosphere formation assay to get a more representative view of how the compound effects cancer cells forming 3D spheroids. MDA-MB 468 cells were plated in a six-welled plate in mammocult media at a density of 4,000 cells/well. The following day the cells were treated with AuBz2 at 2 μM and another group was left untreated as a control. The cells were incubated at 37°C (with supplemental CO_2) for 6 days (144 h). Images of the spheroids were taken at 3 days and 6 days posttreatment (Figure 6A) and the area was calculated using ImageJ processing software then plotted as %area relative to control with GraphPad Prism 10.2.3 (Figure 6B,C). At both the 72 hr and 144 h mark, a statistically significant decrease in spheroid area was observed for the 2 μM group compared to the control with an increase in area of control and decrease in area of the treated group as time proceeds. Thus, AuBz2 is cytotoxic at both the monolayer level and the 3D level, where it inhibits mammosphere formation at low concentrations. AuBz2 was also evaluated in noncancerous HEK293 cells using a 3D spheroid assay. Treatment with 2 μM AuBz2 reduced spheroid formation relative to untreated controls, confirming that the compound retains biological activity in nontransformed cells. Although AuBz2 exhibited activity in HEK293 cells, differences in proteostasis demand, redox state, biodistribution, and stress adaptation between malignant and nonmalignant cells may influence therapeutic response in vivo. Further studies will be required to define the selectivity profile under physiologically relevant conditions.

To understand what may be influencing cell death among this class of compounds, we first measured the production of mitochondrial ROS. The experiment was performed in MDA-MB 468 cells following the treatment of AuBz2 for 2 h at 10 μM. To quantify ROS generation, the cells were stained with the MitoSox Red dye posttreatment and fluorescence was measured using fluorescence-assisted cells sorting (FACS) (Figure 6D,E). We observed a significant increase of ROS production following a 10 μM treatment compared to the control (DMSO). In a rescue experiment, we tested the ROS production of AuBz2 at 5 μM with and without a pretreatment (1 h) of Mito-TEMPO (10 μM), a radical scavenger (Figure 6F,G). The pretreatment of Mito-TEMPO led to a significant decrease of ROS production of AuBz2 at 5 μM, demonstrating a rescue.

Next, we investigated the effect of AuBz2 on mitochondrial membrane potential (MMP), as gold(III) complexes are known to disrupt mitochondrial polarization. To do so, we employed the lipophilic cationic dye tetramethylrhodamine ethyl ester (TMRE), which selectively accumulates within polarized mitochondria due to the negative membrane potential across the inner mitochondrial membrane. MDA-MB-468 cells were treated with increasing concentrations of AuBz2 (5 and 10 μM) for 2 h, followed by TMRE staining and flow cytometric analysis. As shown in Figure 6E–F, AuBz2 induced a dose-dependent decrease in TMRE mean fluorescence intensity (MFI) relative to control cells, indicating progressive depolarization of the mitochondrial membrane. At 10 μM, TMRE fluorescence was

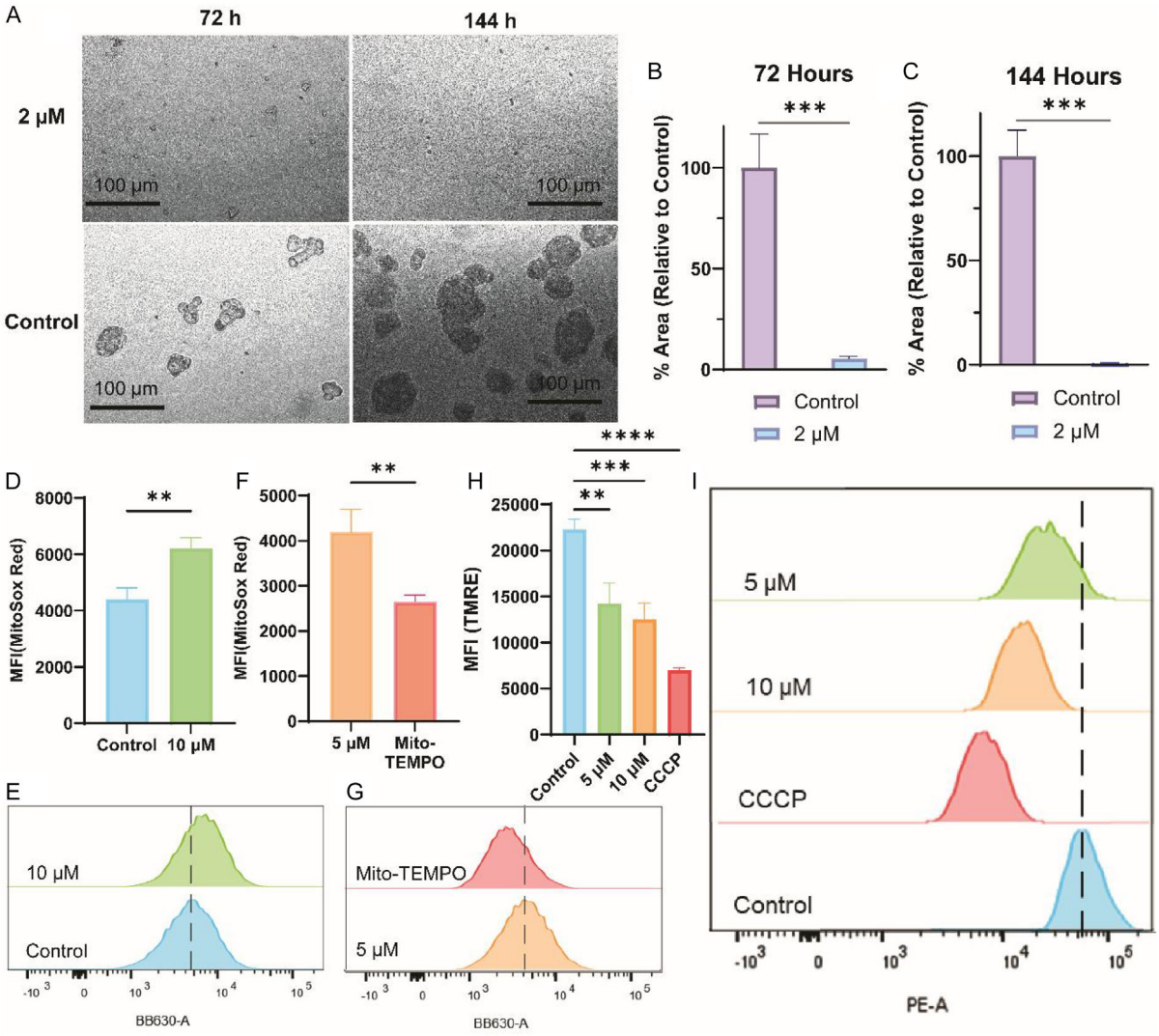

FIGURE 6 | In MDA-MB-468 cells, AuBz2 inhibits mammosphere formation at 2 μM (A–C), induces mitochondrial ROS production with rescue by Mito-TEMPO (D–G), and causes a dose-dependent depolarization of the MMP (H and I). (A) Pictures of mammospheres at 40x magnification 6 days posttreatment with AuBz2 at 2 μM and control (no treatment). (B) Mammosphere area (μm2) plotted as % area relative to control at 72 h posttreatment and (C) 144 h posttreatment with AuBz2. (D) Quantification of MitoSOX Red MFI 2 h after AuBz2 treatment (10 μM) relative to control. (E) Representative flow cytometry histograms corresponding to control and 10 μM AuBz2, with dashed line indicating population median of control. (F) MFI quantification showing mitochondrial ROS following AuBz2 treatment (5 μM) and significant attenuation upon 1 h Mito-TEMPO pretreatment, indicating a rescue effect. (G) Representative histograms for 5 μM AuBz2 with and without Mito-TEMPO pretreatment. (H) MFI quantification showing a dose dependent depolarization of MMP, and (I) representative flow cytometry histograms corresponding to control (no treatment, blue), CCCP (positive control, red), and 10 μM (orange) and 5 μM (green) AuBz2 treatments, with the dashed line indicating population median of control. For B, C, D, and F unpaired *t*-test, $^{*}p < 0.05$ $^{**}p < 0.01$, $^{***}p < 0.001$, $^{****}p < 0.0001$. For H ordinary one-way ANOVA,$^{*}p < 0.05$ $^{**}p < 0.01$, $^{***}p < 0.001$, $^{****}p < 0.0001$. MFI = Mean fluorescence intensity; MMP = mitochondrial membrane potential.

significantly reduced and approached levels observed with the positive control CCCP, confirming substantial loss of $\Delta\Psi m$. These findings demonstrate that AuBz2 disrupts mitochondrial polarization in a concentration-dependent manner, which accompanies ROS production and supports the case for a mitochondrial dysfunction-based mechanism.

2.6 | Impact of AuBz2 on Mitochondrial Bioenergetics

To gain further insight into the mitochondrial effects induced by AuBZ2, we performed a mitochondrial bioenergetics study using the Seahorse XF96 MitoStress assay. The assay consisted of growing MDA-MB 468 cells overnight and then pneumatically injecting AuBz2 at concentrations of 1, 5, and 10 μM prior to analysis. Compound injection was followed by a complex V inhibitor—oligomycin (1.5 μM), an OxPhos uncoupling protonophore—FCCP (0.6 μM), and complex I/III inhibitors rotenone/antimycin A (0.5 μM). All concentrations of AuBz2 produced a significant acute response by increasing oxygen consumption rate (OCR) compared to control, with the 10 μM concentration being the most prominent, increasing more than 450% prior to oligomycin injection (Figure 7B). Postoligomycin injection, the OCR decreased for a few minutes for the control, 1 μM, and 5 μM then

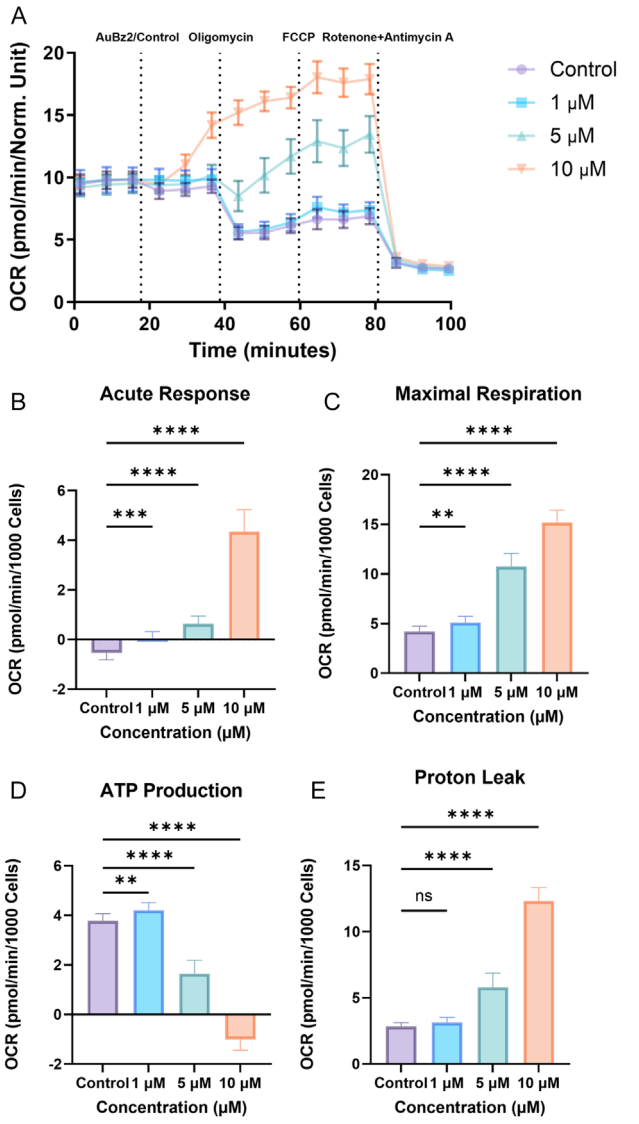

FIGURE 7 | AuBz2 induces mitochondrial uncoupling and bioenergetic disruption in MDA-MB-468 cells. (A) Representative Seahorse F96 MitoStress assay trace showing OCR following sequential injection of AuBz2 (1, 5, and 10 μM), oligomycin (1.5 μM), FCCP (0.6 μM), and rotenone/antimycin A (0.5 μM). AuBz2 elicited a dose-dependent acute increase in OCR, with 10 μM producing the most pronounced response. (B) Quantification of the acute OCR response following AuBz2 injection. (C) Maximal respiration following FCCP injection. (D) ATP-linked respiration calculated from oligomycin-sensitive OCR. (E) Proton leak derived from oligomycin-insensitive OCR. Statistical analysis: Ordinary one-way ANOVA with appropriate multiple comparisons; $*p < 0.05$, $**p < 0.01$, $***p < 0.001$, $****p < 0.0001$; ns = not significant. OCR = Oxygen consumption rate.

steadily increased. However, the 10 μM concentration never decreased in OCR, continuing to rise up to FCCP injection. The increase in OCR following ATP synthase inhibition is a classical signature of OxPhos uncoupling. The uncoupling is further supported by the dose-dependent increase in maximal respiration (Figure 7C) and proton leak (Figure 7E), and decrease in ATP production (Figure 7D). Furthermore, this uncoupling phenotype is consistent with the parallel increase in mitochondrial superoxide and loss of membrane potential observed in MitoSOX and TMRE assays. AuBz2 significantly elevated mitochondrial ROS, which was attenuated by Mito-TEMPO, and induced a dose-dependent collapse of $\Delta\Psi m$. Together, these findings indicate that AuBz2 disrupts mitochondrial bioenergetics through oxidative stress–associated membrane depolarization and impaired coupling efficiency.

3 | Conclusion

This work demonstrates a correlation between the electronics and geometry of gold(III) bisphosphine macrocycles and their potency against triple-negative and estrogen receptor–positive breast cancers. We show that sufficient electron donation to the gold center via the arylbridge atom is necessary for optimizing square planar geometry, enhancing Au–P covalency, stability, and biological activity of the macrocycles, as seen for AuBz2 (O-bridge). Whereas too much electron flow to the metal center, as in the case of AuBz1 (NH-bridge), there is distortion, destabilization, and loss of activity. Furthermore, we demonstrate that square planarity alone does not increase stability or biological activity, as evidenced by AuBz4 (No-bridge).

DFT calculations support the role electronics play on stability and activity, as complexes with greater electron-donating bridging atoms (AuBz1 and AuBz2) display HOMO energies higher than the other derivatives, and are localized on the aryl ligand. The slightly raised HOMO of AuBz2 seems to enhance its stability, whereas the significantly raised HOMO of AuBz1 seems to have a detrimental effect on its stability.

Mechanistic investigations of the lead compound AuBz4 revealed that its anticancer activity is associated with mitochondrial dysfunction, characterized by increased mitochondrial superoxide production, loss of MMP, elevated oxygen consumption, increased proton leak, and reduced ATP-linked respiration. These findings indicate that AuBz4 induces oxidative mitochondrial stress and impairs oxidative phosphorylation coupling in breast cancer cells.

Taken together, these results demonstrate that subtle differences in ligand electronics dictate complex geometry and alter the physicochemical properties, impacting the biological activity of Au(III) bisphosphine macrocycles. This work expands on the rationale design of gold(III) bisphosphine macrocycles by identifying "electronic tuning" of the aryl ligand as a key design feature to promote square planar character and stability of the complex, which governs biological activity. These guiding principles provide valuable insight for the development of next-generation bisphosphine gold(III) macrocycles as anticancer agents.

Acknowledgments

This research was funded by the National Cancer Institute (Award R01CA258421) to S.G.A. The authors gratefully acknowledge the support of various facilities at the University of Kentucky including the UK NMR Center (NSF-CHE-997738) and the UK X-Ray facility (NSF-CHE-1625732). We would like to thank Savita Sharma Ph.D. for the support with our mitostress experiments. This research was supported by the Redox Metabolism Shared Resource of the University of Kentucky Markey Cancer Center (P30CA177558). This work was supported by the UK Flow Cytometry & Immune Monitoring core facility. The authors also acknowledge the support of the Center for Pharmaceutical Research

and Innovation (NIH P20GM130456). High-resolution mass spectrometry analysis was performed at the University of Kentucky Research Mass Spectrometry and Proteomics Core facility, supported by the Office of the Vice President of Research. S.R. and C.R. acknowledge the National Science Foundation (NSF-CBET-2527163) for funding the DFT calculations of the metal coordination complexes and acknowledge the University of Kentucky (UK) Center for Computational Sciences and Information Technology Services Research Computing for their support, collaboration, and use of the Lipscomb Compute Cluster and associated research computing resources.

Funding

This study was supported by National Cancer Institute (grant R01CA258421).

Conflicts of Interest

The authors declare no conflicts of interest.

Data Availability Statement

The data that support the findings of this study are available from the corresponding author upon reasonable request. Deposition Number(s): "=www.ccdc.cam.ac.uk/services/structures?id=doi:10.1002/cbic.202500962R1">- 2516917 **(AuBz1),** 2516918 (**AuBz2**), 2516916 (**AuBz3**), 2516915 (**AuBz4**) contain the supplementary crystallographic data for this paper. These data are provided free of charge by the joint Cambridge Crystallographic Data Centre and Fachinformationszentrum Karlsruhe http://www.ccdc.cam.ac.uk/structures Access Structures service.

References

1. E. Driggers, S. Hale, J. Lee, and N. Terrett, "The Exploration of Macrocycles for Drug Discovery-an Underexploited Structural Class," *Nature Reviews Drug Discovery* 7 (2008): 608.

2. C. Zhang, F. Liu, Y. Zhang, and C. Song, "Macrocycles and Macrocyclization in Anticancer Drug Discovery: Important Pieces of the Puzzle," *European Journal of Medicinal Chemistry* 268 (2024): 116234.

3. L. A. Wessjohann, E. Ruijter, D. Garcia-Rivera, and W. Brandt, "What Can a Chemist Learn from nature?s Macrocycles? A Brief, Conceptual View," *Molecular Diversity* 9 (2005): 171.

4. D. Garcia Jimenez, V. Poongavanam, and J. Kihlberg, "Macrocycles in Drug Discovery—Learning from the Past for the Future," *Journal of Medicinal Chemistry* 66 (2023): 5377.

5. A. S. Arojojoye, J. Holmes, O. A. Obisesan, S. Parkin, and S. G. Awuah, "Stoichiometry Effect on the Structure, Coordination and Anticancer Activity of Gold(I/III) Bisphosphine Complexes," *Dalton Transactions (Cambridge, England: 2003)* 54 (2025): 2018.

6. B.Đ. Glišić and M. I. Djuran, "Gold Complexes as Antimicrobial Agents: an Overview of Different Biological Activities in Relation to the Oxidation State of the Gold Ion and the Ligand Structure," *Dalton Transactions (Cambridge, England: 2003)* 43 (2014): 5950.

7. T. Zou, C. T. Lum, C.-N. Lok, J.-J. Zhang, and C.-M. Che, "Chemical Biology of Anticancer Gold(III) and Gold(I) Complexes," *Chemical Society Reviews* 44 (2015): 8786.

8. R. P. Herrera and M. C. Gimeno, "Main Avenues in Gold Coordination Chemistry," *Chemical Reviews* 121 (2021): 8311.

9. L. Rocchigiani and M. Bochmann, "Recent Advances in Gold(III) Chemistry: Structure, Bonding, Reactivity, and Role in Homogeneous Catalysis," *Chemical Reviews* 121 (2021): 8364.

10. R. T. Mertens, S. Gukathasan, A. S. Arojojoye, C. Olelewe, and S. G. Awuah, "Next Generation Gold Drugs and Probes: Chemistry and Biomedical Applications," *Chemical Reviews* 123 (2023): 6612.

11. R. Wai-Yin Sun, Strategies to Improve the Anti-Cancer Properties of Gold(III) Complexes, *Modern Chemistry & Applications* 1 (2013): 102.

12. P. C. J. Kamer, P. W. N. M. van Leeuwen, and J. N. H. Reek, Wide Bite Angle Diphosphines: Xantphos Ligands in Transition Metal Complexes and Catalysis, *Accounts of Chemical Research* 34 (2001): 895.

13. S. T. Gilpatrick, O. A. Obisesan, S. Parkin, and S. G. Awuah, "Carbon–phosphorus Stapled Au(I) Anticancer Agents *via* Bisphosphine Induced Reductive Elimination," *Dalton Transactions* 53 (2024): 18974.

14. S. Gukathasan, C. Olelewe, L. Ratliff, et al., "Chemoproteomic Profiling of a Carbon-Stabilized Gold(III) Macrocycle Reveals Cellular Engagement with HMOX2," *Journal of Medicinal Chemistry* 68 (2025): 5687.

15. Y. Yang, L. Eberle, F. F. Mulks, et al., "Trans Influence of Ligands on the Oxidation of Gold(I) Complexes," *Journal of the American Chemical Society* 141 (2019): 17414.

16. M. S. M. Holmsen, A. Nova, and M. Tilset, "Cyclometalated (N,C) Au(III) Complexes: The Impact of Trans Effects on Their Synthesis, Structure, and Reactivity," *Accounts of Chemical Research* 56 (2023): 3654.

17. P. Dierkes and P. W. N. M. Van Leeuwen, "The Bite Angle Makes the Difference: A Practical Ligand Parameter for Diphosphine Ligands," *Journal of the Chemical Society, Dalton Transactions* (1999): 1519.

18. B. Pinter, V. Van Speybroeck, M. Waroquier, P. Geerlings, and F. De Proft, "Trans Effect and Trans Influence: Importance of Metal Mediated Ligand–ligand Repulsion," *Physical Chemistry Chemical Physics* 15 (2013): 17354.

19. P. Das, S. Roy, C. Das, R. Biswas, N. Chaterjee, and J. Dinda, Structure-based Design to Explore the Anticancer Efficacy of Organometallic Pt (II)-and Au (III)-n-heterocyclic Carbene (NHC) Complexes, *New Journal of Chemistry = Nouveau Journal De Chimie* 48 (2024): 16189.

20. P. Sahu, N. C. Jana, A. Das, N. Chatterjee, K. Gach-Janczak, and J. Dinda, "Mitochondria-Mediated Anti-Proliferation of Triple-Negative Breast Cancer Cells by Pd(II)–, Pt(II)–, and Au(III)–NHC Complexes of NCN Pincers," *Dalton Transactions (cambridge, England: 2003)* 54 (2025): 10003.

21. S. Gukathasan, S. Parkin, and S. G. Awuah, "Cyclometalated Gold(III) Complexes Bearing DACH Ligands," *Inorganic Chemistry* 58 (2019): 9326.

22. W.-P. To, G. S. M. Tong, C.-W. Cheung, C. Yang, D. Zhou, and C.-M. Che, "Luminescent Cyclometalated Gold(III) Alkyl Complexes: Photophysical and Photochemical Properties," *Inorganic Chemistry* 56 (2017): 5046.

23. L. Messori, L. Massai, F. Fabrizi de Biani, and M. Corsini, "Ligand-Driven Redox Behavior of Gold(III) Complexes: Electrochemical Insights into Stability and Biological Potential," *Polyhedron* 281 (2025): 117730.

24. E. Kimura, Y. Kurogi, and T. Takahashi, "The First Gold(III) Macrocyclic Polyamine Complexes and Application to Selective Gold(III) Uptake," *Inorganic Chemistry* 30 (1991): 4117.

25. L. Messori, F. Abbate, G. Marcon, et al., "Gold(III) Complexes as Potential Antitumor Agents: Solution Chemistry and Cytotoxic Properties of Some Selected Gold(III) Compounds," *Journal of Medicinal Chemistry* 43 (2000): 3541.

26. S. Burger, B. Therrien, and G. Süss-Fink, "1,2-Bis- *N* -[2′-(diphenylphosphanyl)benzoyl]diaminobenzene, a New Chelating Ligand with Versatile Coordination Properties," *European Journal of Inorganic Chemistry* (2003): 3099.

27. N. L. Fry, M. J. Rose, C. Nyitray, and P. K. Mascharak, "Facile Ligand Oxidation and Ring Nitration in Ruthenium Complexes Derived from a Ligand with Dicarboxamide-N and Phosphine-P Donors," *Inorganic Chemistry* 47 (2008): 11604.

28. D. N. Huh, J. B. Gibbons, R. S. Haywood, et al., "Metal-Amidato Complexes: Synthesis, Characterization, and Reactivity of a

Diamidato-Bis(phosphine) Nickel(II) Complex," *Inorganica Chimica Acta* 423 (2014): 290.

29. S. Burger, B. Therrien, and G. Süss-Fink, "Square-Planar Carbonylchlororhodium(I) Complexes Containing *Trans* -Spanning Diphosphine Ligands as Catalysts for the Carbonylation of Methanol," *Helvetica Chimica Acta* 88 (2005): 478.

30. L. Yang, D. R. Powell, and R. P. Houser, "Structural Variation in Copper(I) Complexes with Pyridylmethylamide Ligands: Structural Analysis with a New Four-Coordinate Geometry Index, τ_4," *Dalton Transactions (cambridge, England: 2003)* (2007): 955.

31. J. N. Murrell, "The Electronic Spectrum of Aromatic Molecules VI: The Mesomeric Effect," *Proceedings of the Physical Society. Section A* 68 (1955): 969.

32. Y. Wang, Q.-Y. He, R. W.-Y. Sun, C.-M. Che, and J.-F. Chiu, "Gold(III) Porphyrin 1a Induced Apoptosis by Mitochondrial Death Pathways Related to Reactive Oxygen Species," *Cancer Research* 65 (2005): 11553.

33. Y. F. To, R. W. Y. Sun, Y. Chen, et al., "Gold(III) Porphyrin Complex Is More Potent than Cisplatin in Inhibiting Growth of Nasopharyngeal Carcinoma *In Vitro* and *In Vivo*," *International Journal of Cancer* 124 (2009): 1971.

34. C.-M. Che, R. Sun, W.-Y. Yu, C.-B. Ko, N. Zhu, and H. Sun, Gold(III) Porphyrins as a New Class of Anticancer Drugs: Cytotoxicity, DNA Binding and Induction of Apoptosis in Human Cervix Epitheloid Cancer Cells, *Chemical Communications* 9 (2003): 1718.

35. K. J. Akerman, A. M. Fagenson, V. Cyril, et al., "Gold(III) Macrocycles: Nucleotide-Specific Unconventional Catalytic Inhibitors of Human Topoisomerase I," *Journal of the American Chemical Society* 136 (2014): 5670.

Supporting Information

Additional supporting information can be found online in the Supporting Information section. **Supporting Fig. S1**: Crystal structure of **AuBz1**. Thermal ellipsoids are shown at the 50% probability level. Hydrogen and solvent molecules are omitted for clarity. Only one representative molecule from the asymmetric unit is shown. **Supporting Fig. S2**: Crystal structure of **AuBz2**. Thermal ellipsoids are shown at the 50% probability level. Hydrogen and solvent molecules are omitted for clarity. Only one representative molecule from the asymmetric unit is shown. **Supporting Fig. S3**: Crystal structure of **AuBz3**. Thermal ellipsoids are shown at the 50% probability level. Hydrogen and solvent molecules are omitted for clarity. Only one representative molecule from the asymmetric unit is shown. **Supporting Fig. S4**: Crystal structure of **AuBz4**. Thermal ellipsoids are shown at the 50% probability level. Hydrogen and solvent molecules are omitted for clarity. Only one representative molecule from the asymmetric unit is shown. **Supporting Fig. S5**: ^{1}H NMR of dichloro(2-anilinopyridine)gold(III) in DMSO-d_6 O N Au Cl Cl at 298 K. **Supporting Fig. S6**: 1H NMR of Dichloro(2-Phenoxypyridine)gold(III) in Das determined at the ωB97X-D2/LANL2DZ (CPCM water) level of theory. **Supporting Fig. S7**: 13C NMR of dichloro(2-phenoxypyridine)gold(III) in CDCl3 at 298 K. **Supporting Fig. S8**: 1H NMR of dichloro(2-benzylpyridine)gold(III) in DMSO-d_6 at 298 K. **Supporting Fig. S9**: ^{1}H NMR of *N*, *N*'-(1,2-phenylene)bis(2-(diphenylphosphino)benzamide) in Das determined at the ωB97X-D2/LANL2DZ (CPCM water) level of theory. · **Supporting Fig. S10**: ^{31}P NMR of *N*,*N*'-(1,2-phenylene)bis(2-(diphenylphosphino)benzamide) in DMSO-d_6 at 298 K. **Supporting Fig. S11**: 13C NMR of *N*,*N*' -(1,2-phenylene)bis(2-(diphenylphosphino)benzamide) in Das determined at the ωB97X-D2/LANL2DZ (CPCM water) level of theory. **Supporting Fig. S12**: 1H NMR of **AuBz1**in CDCl3 at 298 K. **Supporting Fig. S13**: 31P NMR of **AuBz1**in CDCl3 at 298 K. **Supporting Fig. S14**: 1H NMR of **AuBz**2 in CDCl3 at 298 K. **Supporting Fig. S15**: 31P NMR of **AuBz**2 in CDCl3 at 298 K. **Supporting Fig. S16**: 1H NMR of **AuBz**3 in CDCl3 at 298 K. **Supporting Fig. S17**: 31P NMR of **AuBz**3 in CDCl3 at 298 K. **Supporting Fig. S18**: 1H NMR of **AuBz**4 in CDCl3 at 298 K. **Supporting Fig. S19**: 31P NMR of **AuBz**4 in CDCl3 at 298 K. **Supporting Fig. S20**: HPLC Trace of *N*,*N*'-(1,2-phenylene) bis(2-(diphenylphosphino)benzamide) λ = 280 nm). **Supporting Fig. S21**: HPLC Trace of **AuBz**1 (λ = 280 nm). **Supporting Fig. S22**: HPLC Trace of **AuBz**2 (λ = 260 nm). **Supporting Fig. S23**: HPLC Trace of **AuBz3** (λ = 260 nm). **Supporting Fig. S24**: HPLC Trace of **AuBz4** (λ = 260 nm). **Supporting Fig. S25**: ESI+ of *N*,*N*'-(1,2-phenylene)bis(2-(diphenylphosphino)benzamide). **Supporting Fig. S26**: ESI+ **AuBz1. Supporting Fig. S27**: ESI+ **AuBz2**. **Supporting Fig. S28**: Zoomed ESI+ **AuBz2**. **Supporting Fig. S29**: ESI+ **AuBz3**. **Supporting Fig. S30**: ESI+ **AuBz4. Supporting Fig. S31**: HRMS of **AuBz1. Supporting Fig. S32**: HRMS of **AuBz2**. **Supporting Fig. S33**: HRMS of **AuBz3**. **Supporting Fig. S34a**: HRMS of **AuBz4. Supporting Fig. S34b**: **AuBz1** Calculated and found HRMS isotopes and Δ and mass error (ppm) calculations. **Supporting Fig. S35**: **AuBz2** Calculated and found HRMS isotopes and Δ and mass error (ppm) calculations. **Supporting Fig. S36**: **AuBz3** Calculated and found HRMS isotopes and Δ and mass error (ppm) calculations. **Supporting Fig. S37**: **AuBz4** Calculated and found HRMS isotopes and Δ and mass error (ppm) calculations. **Supporting Fig. S38**: HPLC traces of **AuBz2** from 0 to 48 h in DMEM. **Supporting Fig. S39a**. HPLC traces of **AuBz2** from 0 to48 h in DMEM with corresponding isotope species. **Supporting Fig. S39b**. ESI-MS of 1—Intact compound (Peak A, species A) and 2—Intact compound (Peak C, species A, B, C). **Supporting Fig. S40**: HPLC traces of **AuBz2** from 0 to 48 h in H_2O. **Supporting Fig. S41**: A—HPLC traces of **AuBz2** from 0 to 48 h in the presence of 5 equiv of GSH. B—Mass spectrum of **AuBz2** at time 0 h. C—Mass spectrum of **AuBz2** at time 48 h. **Supporting Fig. S42**: Cyclic voltammogram of **AuBz1. Supporting Fig. 43**: Cyclic voltammogram of **AuBz2**. **Supporting Fig. S44**: Cyclic voltammogram of **AuBz3**. **Supporting Fig. S45**: Dose response curve of **AuBz1**, **AuBz2,** and **AuBz3** in SUM159. **Supporting Fig. S46**: Dose response curve of **AuBz1**, **AuBz2** and **AuBz3** in MDA-MB 468. **Supporting Fig. S47**: Dose response curve of **AuBz1**, **AuBz2** and **AuBz3** in MDA-MB 231. **Supporting Fig. S48**: Dose response curve of **AuBz1**, **AuBz2,** and **AuBz3** in MCF7. **Supporting Fig. S49**: Dose response curve of **AuBz4** in MDA-MB 468, SUM 159, MCF7, and MDA-MB 231. **Supporting Fig. S50**: Dose response curve of **Cisplatin** in MDA-MB 231, MDA-MB 468, and SUM 159. **Supporting Fig. S51**: Dose response curve of **dppbH$_2$** in MDA-MB 468. **Supporting Fig. S52**: Bar graphs depicting IC_{50} values for the macrocycles and cisplatin. **Supporting Fig. S53**: Graph of HOMO–LUMO energy gaps for the C^N cyclometalated ligands. **Supporting Fig. S54**: Graph of HOMO–LUMO energy gaps for the four macrocyclic complexes. **Supporting Fig. S55**: Top view of HOMO and LUMO electronic density maps of cyclometalated ligands as determined at the ωB97X-D2/LANL2DZ (CPCM water) level of theory (isovalue = 0.04). **Supporting Fig. S56**: Side view of HOMO and LUMO electronic density maps of cyclometalated ligands as determined at the ωB97X-D2/LANL2DZ (CPCM water) level of theory (isovalue = 0.04). **Supporting Fig. S57**: View 1, HOMO and LUMO electronic density maps of the macrocyclic complexes.Level of theory ωB97X-D2/LANL2DZ (CPCM water) isovalue = 0.04. **Supporting Fig. S58**: View 2, HOMO and LUMO electronic density maps of the macrocyclic complexes.Level of theory ωB97X-D2/LANL2DZ (CPCM water) isovalue = 0.04. **Supporting Table S1**: X-ray Parameters of **AuBz1**, **AuBz2**, **AuBz3**, and **AuBz4** Macrocycles. **Supporting Table S2**: Selected bond lengths (Å) and bond angles (°) for Au(III) macrocycles **AuBz1**, **AuBz2**, **AuBz3**, and **AuBz4** determined by X-ray crystallography. **Supporting Table S3**: Bond lengths (Å) of Au–C, Au–Cl, Au–P, and average Au–P for the 4 macrocycles as determined at the ωB97X-D2/LANL2DZ (CPCM water) level of theory. **Supporting Table S4**: Angles for the four macrocycles as determined at the ωB97X-D2/LANL2DZ (CPCM water) level of theory. **Supporting Table S5**: Mulliken charges as determined at the ωB97X-D2/LANL2DZ (CPCM water) level of theory. **Supporting Table S6**: Calculated binding energies for cyclometalated ligand to Au(III) complexes represented with electron energies as determined at the ωB97X-D2/LANL2DZ (CPCM water) level of theory. **Supporting Table S7**: Calculated binding energies for cyclometalated ligand to Au(III) complexes represented with zero-point energy and thermal enthalpy corrections as determined at the ωB97X-D2/LANL2DZ (CPCM water) level of theory.